

See discussions, stats, and author profiles for this publication at: <https://www.researchgate.net/publication/264395454>

Gradient $\text{FeOx}(\text{PO}_4)(y)$ Layer on Hematite Photoanodes: Novel Structure for Efficient Light-Driven Water Oxidation

ARTICLE in ACS APPLIED MATERIALS & INTERFACES · JULY 2014

Impact Factor: 6.72 · DOI: 10.1021/am502821d · Source: PubMed

CITATIONS

3

READS

44

9 AUTHORS, INCLUDING:



Yuchao Zhang

Chinese Academy of Sciences

3 PUBLICATIONS 23 CITATIONS

SEE PROFILE



Chuncheng Chen

Chinese Academy of Sciences

111 PUBLICATIONS 5,600 CITATIONS

SEE PROFILE



Wanhong Ma

Chinese Academy of Sciences

117 PUBLICATIONS 5,795 CITATIONS

SEE PROFILE

Gradient $\text{FeO}_x(\text{PO}_4)_y$ Layer on Hematite Photoanodes: Novel Structure for Efficient Light-Driven Water Oxidation

Yuchao Zhang,[†] Zichao Zhou,[†] Chuncheng Chen,^{*,†} Yanke Che,[†] Hongwei Ji,[†] Wanhong Ma,[†] Jing Zhang,[‡] Dongyan Song,[‡] and Jincai Zhao[†]

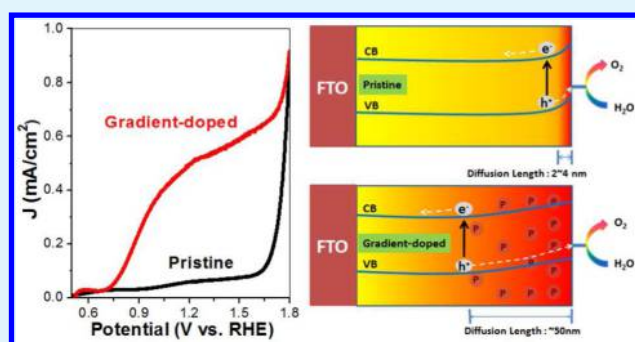
[†]Key Laboratory of Photochemistry, Beijing National Laboratory for Molecular Sciences, Institute of Chemistry, Chinese Academy of Sciences, Beijing 100190, China

[‡]Beijing Synchrotron Radiation Facility (BSRF), High Energy Institute of Physics, Chinese Academy of Sciences, Beijing 100049, China

S Supporting Information

ABSTRACT: Hematite has been receiving increasing attention for its application in photoelectrochemical (PEC) water oxidation but usually exhibits poor efficiency. We fabricated a stable gradient-structured $\text{FeO}_x(\text{PO}_4)_y$ layer on hematite by diffusively incorporating phosphate onto the surface layer of hematite films at a low temperature. X-ray photoelectron spectroscopy depth profile and Fe K-edge grazing-incidence X-ray absorption near-edge structure and extended X-ray absorption fine structure analysis demonstrated the formation of a ~ 50 nm overlayer with a gradient phosphorus distribution and structural evolution from the outer surface to the depth. The as-prepared photoanodes showed highly improved PEC water oxidation performance. Up to 8.5-fold enhancement in the photocurrent density at 1.23 V versus reversible hydrogen electrode was achieved relative to the pristine anode. This strategy is applicable for hematite photoanodes prepared by different methods and with different morphologies and structures. The improvement in the water oxidation activity is mainly attributed to the enhanced separation of photogenerated electron–hole pairs, which is derived from the increased hole diffusion length in the gradient-structured overlayer. This work develops a simple and universal method to boost the PEC water oxidation efficiency with versatile hematite photoanodes.

KEYWORDS: hematite, gradient, $\text{FeO}_x(\text{PO}_4)_y$, water oxidation, hole diffusion length



INTRODUCTION

Hematite ($\alpha\text{-Fe}_2\text{O}_3$) is a promising material for photoelectrochemical (PEC) water splitting because of its distinct merits such as abundance, nontoxicity, stability, and favorable optical band gap (~ 2.2 eV, with a theoretical solar-to-hydrogen efficiency of up to 16.8%).^{1,2} Notwithstanding its appeal, hematite has several intrinsic drawbacks:¹ (1) a short hole diffusion length (only $\sim 2\text{--}4$ nm) relative to the long penetration depth of light (ca. 100 nm with photon energy close to E_g); (2) low electron mobility ($\sim 10^{-1}$ $\text{cm}^2 \text{V}^{-1} \text{s}^{-1}$); (3) high overpotentials for water oxidation. Many strategies have been developed to address these problems. For example, the overpotential can largely be reduced by surface loading water oxidation catalysts (WOCs), such as cobalt phosphate (Co-Pi),^{3–5} IrO_2 ,⁶ and CoO_x ,⁷ to accelerate the water oxidation kinetics or by passivating the surface trapping states with Al_2O_3 .⁸ The electron mobility can be greatly enhanced by doping with elements such as Si^{4+} ,⁹ Ti^{4+} ,¹⁰ and Sn^{4+} .^{11,12} However, methods to increase the hole diffusion length of the hematite photoanode have not been explored much.

In principle, the fabrication of heterojunction structures (e.g., p–n junctions) on the surface of semiconductors can increase the carrier diffusion length by creating a built-in field near the interface.^{13,14} For example, Wang and co-workers deposited a magnesium-doped p-type hematite overlayer on the surface of $\alpha\text{-Fe}_2\text{O}_3$ by atomic layer deposition and observed a nominal 200 mV cathodic shift of the onset potential.¹³ Cobalt-doped $\alpha\text{-Fe}_2\text{O}_3$ nanorod/ MgFe_2O_4 heterojunctions formed at a high temperature (550 °C), and a long annealing time (10 h) has also been reported by Feng and co-workers to exhibit more efficient PEC water oxidation.¹⁴ In such p–n junctions, there exists an obvious interface between the p- and n-type components,^{13,14} and the built-in field is localized only in the narrow interface region. Hence, the increase in the hole diffusion length is still limited.

Phosphate (Pi) species have been used to control the shape of $\alpha\text{-Fe}_2\text{O}_3$ particles because of their strong interaction with the

Received: May 7, 2014

Accepted: July 21, 2014

Published: July 21, 2014

surface of α -Fe₂O₃ particles.^{15–18} In this work, we report that the strong interaction between Pi and hematite also provides an opportunity to dope Pi onto the surface layer of hematite under mild conditions. The in situ formed FeO_x(PO₄)_y layer was characterized to have a unique gradient structure, which makes this strategy distinguished from both the traditional surface modification by WOCs^{3,4,6,19} and the bulk doping by elements such as Si⁴⁺.⁹ The photoanodes with such a structure exhibited highly improved PEC performance. The relationship between the photoactivity and structure was further discussed in terms of increasing the hole diffusion length by continuously changing the gradient in the built-in field rather than enhancing the water oxidation kinetics or increasing the electron mobility. Our work provides a simple but effective strategy for enhancing the photoinduced electron–hole separation efficiency by increasing the hole diffusion length in hematite photoanodes for water oxidation.

■ EXPERIMENTAL SECTION

Photoanode Preparation. Hematite nanowires were prepared on a fluorine-doped tin oxide (FTO; TCO-15, Nippon Sheet Glass, Japan, 14 Ω sq^{−1}) glass substrate by a modified procedure reported by Li and co-workers.¹¹ Briefly, 100 mL of an aqueous solution containing 2.43 g of ferric chloride (FeCl₃·6H₂O; Alfa Aesar, 98%) and 0.85 g of sodium nitrate (NaNO₃; J&K, 99%) at pH 1.4 (adjusted by HCl) was prepared in a Teflon-lined stainless steel autoclave. Several FTO glass slides (2 × 4 cm), washed with acetone, ethanol, and then deionized water, were placed in the autoclave and heated at 95 °C for 4 h. After hydrothermal treatment, a uniform layer of iron oxyhydroxides (FeOOH) was coated on the FTO glass, which was washed completely with deionized water to remove any residual salts. The obtained film was sintered in air at 550 °C for 2 h to convert FeOOH into hematite (abbreviated as NW550). Further annealing of NW550 at 650 °C for 20 min yielded the sample NW650, and annealing of NW550 at 750 °C for 15 min produced the sample NW750.

Tin-doped hematite nanocorals (abbreviated as NC650) were prepared by the same procedure as that used to synthesize the above-mentioned hematite nanowires NW650, except that 1 mL of a tin(IV) chloride (SnCl₄; Alfa Aesar, 98%)/ethanol solution (10 mg mL^{−1}) was added as the tin precursor to the solution mixture before the hydrothermal process.¹⁰ Boron-doped hematite nanowires (BNW650) were prepared by adding Na₂B₄O₇ as the precursor.

Electrodeposited hematite films (abbreviated as ED650) were prepared on FTO glass substrates by a procedure based on Spray and Choi's work.²⁰ Electrodeposition was carried out using 100 mL of an aqueous solution containing 0.4 g of FeCl₂·5H₂O (J&K, 99%). FTO was used as the working electrode. A potentiostatical deposition at $E = 1.2$ V versus Ag/AgCl (average deposition current density of 0.5 mA cm^{−2}) was carried out at 75 °C for 6 min using an electrochemical workstation (model CHI 760D, CH Instruments, Inc.). After deposition, the resulting film was thoroughly rinsed with deionized water to remove any residual salts. The film was subsequently sintered in air at 550 °C for 2 h and for an additional 20 min at 650 °C.

For H₃PO₄ treatment (Pi treatment), the hematite films were soaked in phosphoric acid for 10 min and subsequently heated at different temperatures (optimally 300 °C) for 2 h. The films were then washed completely with deionized water. For comparison, the control hematite films also underwent an identical treatment procedure but without soaking in phosphoric acid.

A hematite film with surface-loaded Co-Pi was also fabricated for comparison, according to the most commonly applied electrodeposition methods.^{3,19} The NW650 film was submerged in a solution of 0.5 mM cobalt nitrate in a 0.1 M potassium phosphate (K-Pi) buffer (pH 7). Co-Pi was electrodeposited at +1.1 V versus Ag/AgCl for 15 min.

PEC Experiments. The PEC performances of the films were examined in the 1 M NaOH electrolyte solution (pH 13.6) in a three-electrode electrochemical cell using hematite films as the working

electrode. A platinum foil was used as the counter electrode, and a KCl-saturated Ag/AgCl electrode was used as the reference electrode. The electrolyte solution was deaerated by purging argon for 30 min before a J – V scan. The measured potentials versus Ag/AgCl were converted to the reversible hydrogen electrode (RHE) scale according to the Nernst equation

$$E_{\text{RHE}} = E_{\text{Ag/AgCl}} + 0.059\text{pH} + E_{\text{Ag/AgCl}}^0$$

where E_{RHE} is the converted potential versus RHE, $E_{\text{Ag/AgCl}}^0 = 0.1976$ V at 25 °C, and $E_{\text{Ag/AgCl}}$ is the experimentally measured potential versus a saturated Ag/AgCl reference electrode. A 150 W xenon lamp coupled to an AM 1.5G filter was used as the white-light source. A light power density of 100 mW cm^{−2} was measured with a radiometer (CEAULIGHT, CEL-NP2000). Incident photon-to-current efficiencies (IPCEs) were measured with a monochromator coupled to the 150 W xenon lamp.

Electrochemical impedance spectroscopy (EIS) spectra were measured under visible-light illumination ($\lambda > 420$ nm; $I_0 = 60$ mW cm^{−2}), recorded by an electrochemical workstation (PGSTAT302N autolab, Metrohm). A sinusoidal voltage pulse with an amplitude of 10 mV was applied on a given bias voltage, with a frequency that ranged from 10 kHz to 1 Hz. Mott–Schottky plots were collected with a bias voltage scanned from −0.4 to 0.1 V versus Ag/AgCl with an interval of 50 mV, in the dark at frequencies ranging from 1000 to 100 Hz. The raw data were fitted using Nova 1.8 software from Metrohm Inc.

Structural Characterization. UV–vis diffuse-reflectance spectra were recorded on a Hitachi U-3010 instrument. X-ray diffraction (XRD) measurements were performed on a Regaku D/Max-2500 diffractometer with a Cu KR radiation source (1.5406 Å). Diffraction patterns were recorded from $2\theta = 10$ to 80° with a step size of 0.04° at 4° min^{−1}. X-ray photoelectron spectroscopy (XPS) data were obtained with an ESCALab220i-XL electron spectrometer from VG Scientific using 300 W Al K α radiation. The base pressure was about 3×10^{-9} mbar. The binding energies were referenced to the C 1s line at 284.8 eV from adventitious carbon. Argon-ion etching was conducted at an argon partial pressure of 2×10^{-7} mbar at 3 kV and 10 mA. Scanning electron microscopy (SEM) data were obtained with a Hitachi S4800 scanning electron microscope (Hitachi Ltd.) operated at an acceleration voltage of 15 kV for the cross-sectional view and 10 kV for the top view. X-ray absorption fine structure (XAFS) experiments were carried out at the XAFS station of the BSRF. The beamline provided a focused X-ray beam with energy ranging from 5 to 20 keV, a photon flux on the order of 10^{11} phs s^{−1} (at 10 keV), and a beam size of 0.9 (H) × 0.3 (V) mm². The energy was calibrated by a standard iron metal foil before each experiment. Fe K-edge grazing-incidence X-ray absorption fine structure (GI-XAFS) spectra of the samples were collected by a Lytle fluorescence detector at room temperature. The grazing angles were tuned from 0.3 to 45° on a stepper-motor-controlled stage with a precision of better than 0.01°. XAFS data were collected from −20 to +60 eV relative to the Fe K-edge. The XAFS data were analyzed using the Athena and Artemis interfaces of the IFEFFIT program package.

■ RESULTS AND DISCUSSION

The primary α -Fe₂O₃ films consisted of hematite nanowires grown perpendicular to the FTO surface, with a diameter of about 50 nm and an average length of 300 nm (Figure S1 in the Supporting Information, SI). The α -Fe₂O₃/FeO_x(PO₄)_y films (abbreviated as Pi anode hereafter) were obtained by simply dipping these α -Fe₂O₃ films into a H₃PO₄ solution (0.1–0.2 M) and then sintering at low temperature (300 °C). The pristine hematite nanowire film is quite resistant to an acidic H₃PO₄ solution. During the 10 min dipping in a 0.1 M H₃PO₄ solution, only 0.4% of the total iron (0.12 μ g/357.8 μ g) was dissolved, as measured by inductively coupled plasma mass spectrometry (Table S1 in the SI). After such Pi treatment, accordingly, SEM images showed no significant variation in the

film morphologies (Figure S1 in the SI) nor did the general XRD patterns change much (Figure S2 in the SI), except that there was some decrease in the relative intensities of the (110) diffraction peaks. These results suggest that Pi treatment adapted in this work does not alter the crystalline structure of bulk hematite but slightly reduces the aspect ratio of the nanowire because of the selective interaction of Pi ions with the (110) facet.^{15–18} The UV–vis spectra (Figure S3 in the SI) indicate that the Pi-treated film exhibited somewhat less absorption in the visible-light region (particularly between 500 and 550 nm) than the untreated one. Because only 0.4% of the total iron was dissolved during Pi treatment, the fading and discoloring of the Pi-treated films result from the lower absorbance of the as-formed $\text{FeO}_x(\text{PO}_4)_y$ species in the visible-light region. However, the onset of visible-light absorption was not changed much, suggesting that the band gap is not influenced much by Pi treatment.

The XPS survey spectra confirmed the presence of phosphorus on the surface of the Pi anode, while no phosphorus signal was detected on the untreated sample (Figure S4A in the SI). For the pristine anode, the Fe $2p_{3/2}$ binding energy of 710.6 eV was fully consistent with the typical values reported for Fe_2O_3 .^{21,22} For the Pi anode, the Fe $2p_{3/2}$ binding energy shifted to 712.4 eV (Figure S4B in the SI), quite close to the values reported for FePO_4 .²³ Accordingly, the O 1s binding energy peak shifted from the typical values for Fe_2O_3 (530.0 eV)^{24,25} for the pristine anode to 531.7 eV for the Pi anode, which was attributed to oxygen atoms of PO_4^{3-} .^{23,26} The P 2p spectrum shows that phosphorus exhibited a binding energy of 133.9 eV, close to the values reported for FePO_4 (133.4 eV).²³ All of these observations indicate that Pi treatment introduces some FePO_4 -like structures on the outermost surface of the Pi anode.

To investigate the phosphorus distribution across the Pi anode, XPS depth profile analysis by argon-ion etching was further performed. As shown in Figure 1A, before argon-ion etching, the atomic percentage of phosphorus was about 16% at the outermost surface, close to the stoichiometric content (16.7%) in FePO_4 . With increasing etching time, the atomic percentage decreased gradually to 10% and then remained unchanged with further etching. The XPS depth profile shows an evident phosphorus gradient structure of the Pi anode with a doping depth of about 50 nm. Although the hematite nanostructure (Figure S1 in the SI) might prevent the completely isotropic argon-ion etching and make it difficult to obtain the exact depth, it is evident that phosphorus is gradually distributed on the top part of the nanowire.

Our XRD results showed that there was some decrease in the relative intensities of the (110) diffraction peaks after Pi treatment (Figure S2 in the SI). It has been reported that Pi ions have strong interaction with the (110) facet of $\alpha\text{-Fe}_2\text{O}_3$ particles.^{15–18} During Pi treatment, hematite was first dipped in a H_3PO_4 solution. In this process, the Pi ions would selectively adsorbed on the (110) planes of hematite particles. The annealing process followed at 300 °C for 2 h would lead to diffusion of Pi ions into the bulk through the (110) facet. As a result, the (110) facet of $\alpha\text{-Fe}_2\text{O}_3$ would be destroyed. This is the reason for the decrease in the relative intensity of the (110) peak.

It was also observed that the binding energy of iron gradually shifted from 712.2 eV on the outermost surface to 710.2 eV (a value similar to that of the surface iron of the pristine anode). After three runs of Ar^+ etching, the binding energies no longer

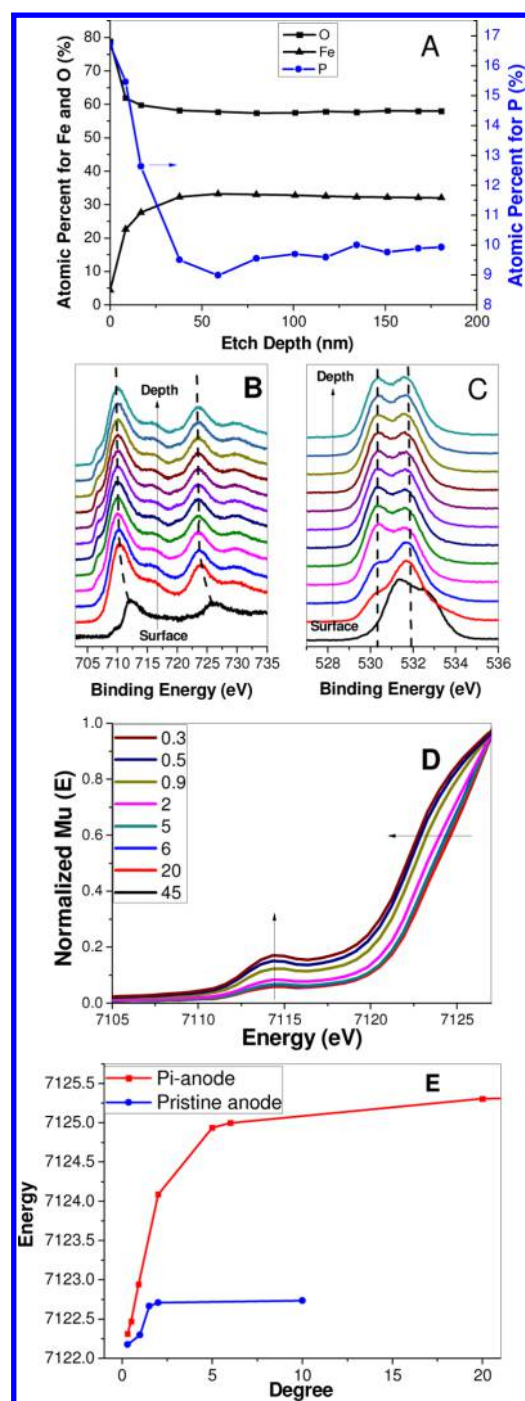


Figure 1. (A) Change in the molar ratios of iron, oxygen, and phosphorus elements with the etching depth in an XPS depth profile for Pi anode obtained by argon-ion etching. The high-resolution XPS results were obtained for (B) Fe $2p_{3/2}$ and (C) O 1s at the corresponding points in part A. (D) Fe K-edge GI-XANES data for the Pi anode. (E) Plot of E_{edge} versus grazing-incidence angles.

changed with further etching (Figure 1B). Similarly, the XPS spectra of O 1s in the depth profile also exhibited a corresponding shift in the binding energies from FePO_4 -like binding energies at the outermost surface to Fe_2O_3 -like ones in the bulk film (Figure 1C). The gradual shifts in the binding energies of iron and oxygen in the Pi anode indicate a gradual change in their structural environments with the film depth rather than only a change in the amount of Pi.

To further shed light on the change in the structure and component at the surface layer of the Pi anode, X-ray absorption near-edge structure (XANES) spectra were recorded in the grazing-incidence mode, in which X-rays can reach different depths across the film by tuning the angle of grazing incidence. Theoretically, the penetration depth of the incident X-ray beam could be calculated by the incidence angle. However, the complicated morphology of the nanowire makes it difficult to estimate the quantitative relationship between the penetration depth of the X-rays and the incidence angle because the transport of the X-rays is known to be greatly dependent on the morphology of the film. As shown in Figure 1D, at incidence angles greater than 6° , the XANES spectra were very similar to those obtained in the conventional fluorescence mode (Figure S5 in the SI), and little change was observed with an increase in the incidence angles. It is clear that, at these incidence angles, the XANES spectra reflect the bulk structure of the film because of the deep penetration of the X-rays. Interestingly, at small incident angles ($<6^\circ$), at which X-rays are expected to graze over the surface layers, two notable changes in the XANES spectra can be observed with decreasing angles. First, the preedge peak at 7114.4 eV exhibited a gradual increase. This preedge peak is a signature of the 1s–3d transition of tetrahedral coordinated iron, which is commonly found in Fe_3O_4 (Figure S5 in the SI) and quite weak for $\alpha\text{-Fe}_2\text{O}_3$.²⁷ The larger preedge peak at smaller incident angles suggests that the content of tetrahedral coordinated iron increases gradually toward the surface of the Pi anode. Another significant change in the spectra was the angle dependence of the absorption-edge energy, which is a direct indication of the valence state of the elements. As the angle decreased from 6° to 0.3° , the absorption-edge energies (Figure 1D), and correspondingly the first maxima of the first-order derivative of the absorption coefficient curves (Figure S6A in the SI), shifted toward a lower value by ca. 2.7 eV. The reduced absorption-edge energies indicate an increase in the content of iron in its reduced state (nominally Fe^{2+}) with decreasing depth in the film. As a control experiment, GI-XANES spectra were also recorded for the pristine anode (Figure S6B,C in the SI). Variations in both the absorption-edge energy and the preedge with the incidence angles were rather insignificant, relative to those in the Pi anode (Figure S6B in the SI). Analysis on the first-order derivative of the absorption coefficient curves showed that the first maximum of the derivative for the pristine anode shifted by less than 0.6 eV with the incident angles from 0.3° to 10° (Figures 1E and S6C in the SI), which is much smaller than that of the Pi anode (2.7 eV). Because Pi treatment did not significantly change the morphologies of the anode (Figure S1 in the SI), the different angle-dependent changes in the preedge peak and absorption-edge energy between the pristine and Pi anodes could not be attributed to the morphology changes, and the possibility that these changes originate from the angle-dependent self-absorption could also be ruled out. Rather, the angle dependence of the GI-XANES spectra should stem from the structural change of the surface layer after Pi treatment.

Grazing-incidence extended X-ray absorption fine structure (GI-EXAFS) spectra for the Pi and pristine anodes were further analyzed by Artemis software. The fitted radial structure functions and the corresponding structure information on the first Fe–O coordination are shown in Figure S7 and Table S2 in the SI, respectively. For the pristine hematite structure, well-agreeing with the literature,¹ an iron atom was found to be in a

hexa-O-coordinated environment. For the Pi anode, with incident angles varied from 45° to 0.3° , the coordination number of the oxygen atom decreased from 6.72 to 2.00. This indicates that more oxygen vacancies existed toward the surface of the Pi anode. This result is consistent with the above GI-XANES results that iron was less coordinated by surrounding atoms toward the surface.

A comparison of the distribution of the Pi-doping concentration (Figure 1A) and the change in the XANES (Figure 1D) and EXAFS (Figure S7 in the SI) spectra of iron crossing the film suggests that the changes in the states of iron species were caused by Pi doping. The presence of Pi is essential for the creation and preservation of these reduced iron sites and oxygen vacancies.

Figure 2A shows the PEC water oxidation performances of the representative hematite anodes. The pristine anode exhibited a rather low photocurrent density of only 0.06 mA cm^{-2} at $1.23 \text{ V}_{\text{RHE}}$. The Pi anode showed a dramatic 8.5-fold enhancement in the photocurrent density, up to 0.51 mA cm^{-2} at $1.23 \text{ V}_{\text{RHE}}$. The relative dark current densities are shown in Figure S8 in the SI. Illumination with chopped light also

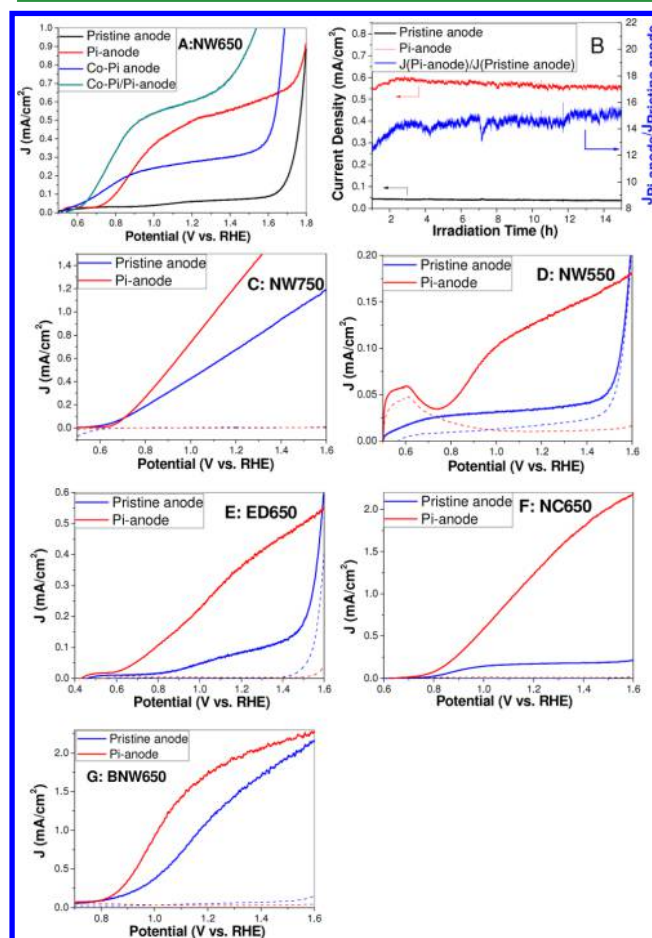


Figure 2. (A) J - V curves for the pristine, Pi-treated, Co-Pi-loaded, and Co-Pi/Pi-cotreated hematite photoanodes under simulated solar illumination in 1 M NaOH at a scan rate of 50 mV s^{-1} . (B) Steady-state photocurrent density obtained at $1.23 \text{ V}_{\text{RHE}}$ over 15 h of PEC water-splitting experiments. (C–G) Effect of Pi treatment on the photocurrent densities for the hematite photoanodes prepared by different methods and with different morphologies. All of the solid lines denote photocurrent densities, while the dashed lines represent the corresponding dark current densities.

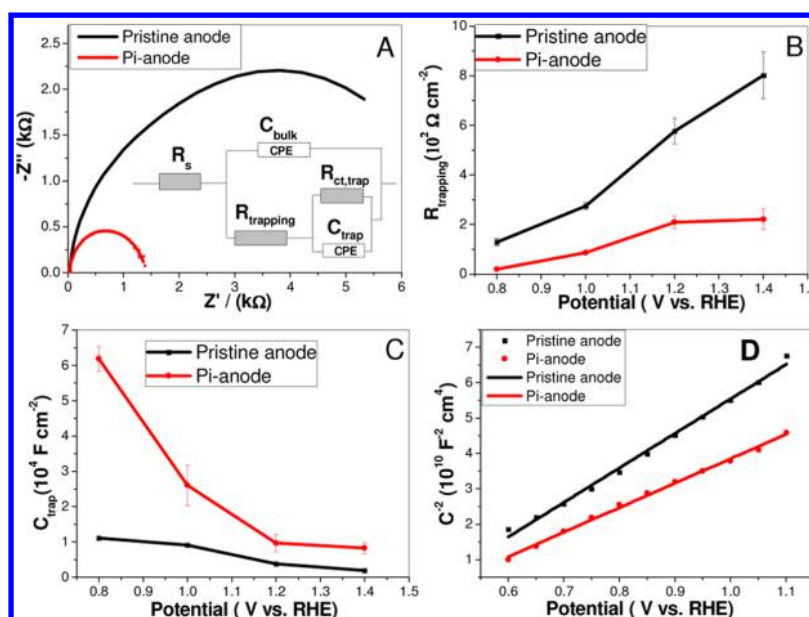


Figure 3. (A) EIS spectra measured at 1.23 V_{RHE} in a 1 M NaOH electrolyte. Inset: equivalent circuit used for the fit and simulation. (B) $R_{trapping}$ and (C) C_{trap} values fitted from EIS data obtained for the pristine and Pi anodes. (D) Mott–Schottky plots collected in the dark.

exhibited a significant photocurrent enhancement of the Pi anode (Figure S9 in the SI). IPCEs were measured at 1.23 V_{RHE} for the pristine and Pi anodes (Figure S10 in the SI). Compared with the pristine anode, the Pi anode exhibited enhanced IPCE values, especially in the incident light wavelength between 350 and 450 nm. At 410 nm, IPCE of the Pi anode reached 9%, nearly 10 times that of the pristine anode. These results are consistent with the J – V scan. It is interesting that in spite of the low visible absorption of the Pi anode (Figure S3 in the SI), the PEC activity still increases significantly, indicating that the $FeO_x(PO_4)_y$ overlayer has an important promoted role, which outplays the decrease in the absorbance.

The as-prepared Pi anode is quite reproducible. As shown in Figure S11 in the SI, four more anodes were synthesized and the photocurrent density at 1.23 V_{RHE} varied between 0.46 and 0.54 mA cm⁻². A control experiment by directly adding 1 M Pi into the electrolyte showed that the enhancement originated from the intrinsic change in the films by Pi treatment and not from the Pi ions in the electrolyte or those simply adsorbed on the film surface (Figure S12 in the SI). The hypothesis that the poor surfaces of the anodes were etched by a H₃PO₄ solution can also be excluded because only very little iron was dissolved during the 10 min dipping in a 0.1 M H₃PO₄ solution; on the other hand, the subsequent annealing temperature can largely affect the activity, and 300 °C was found to be the optimal temperature (Figure S13 in the SI). This means the diffusion process of phosphorus into the hematite structure is of significance for the enhancement.

To investigate the activity and stability of the Pi anode under steady-state conditions, long-term PEC operation was conducted at 1.23 V_{RHE}. As shown in Figure 2B, for the pristine anode, the photocurrent density underwent a gradual decrease from 0.050 to 0.036 mA cm⁻² throughout the entire irradiation time during the PEC experiment. By contrast, for the Pi anode, the photocurrent density continually increased during the first 3 h of irradiation, probably because of passivation of the surface trapping states by anodic healing of the oxygen vacancies under PEC conditions.²⁸ After the healing period, the photocurrent

density on the Pi anode was increased by a factor of up to 15 times that on the pristine one, which was much higher than that obtained by the J – V scan (8.5 times). After the PEC reaction was allowed to proceed for 15 h, about 30.5 and 2.1 C cm⁻² photocharges were generated for the Pi and pristine anodes, respectively.

The universality of the Pi-incorporation strategy by low-temperature diffusion was examined on other hematite photoanodes prepared by different methods and with different morphologies (Figure S14 in the SI) and structures (Figure S15 in the SI). As shown in Figure 2C–G, for all of the Pi-treated hematite anodes, a significant increase in the photocurrent density was observed. The pristine hematite nanowires prepared by hydrothermal methods and sintered at 750 °C (NW750)¹¹ showed a PEC activity of 0.72 mA cm⁻² at 1.23 V_{RHE}. After Pi treatment, the photocurrent density at 1.23 V_{RHE} was nearly doubled (1.30 mA cm⁻²; Figure 2C). The hematite nanowire anode sintered at 550 °C (NW550) exhibited a rather low photocurrent density (0.04 mA cm⁻² at 1.23 V_{RHE}). Pi treatment enhanced the photocurrent density to 0.13 mA cm⁻² (Figure 2D). For the electrodeposition anode (ED650), a 4-fold enhancement in the photocurrent density at 1.23 V_{RHE} was achieved (Figure 2E). The tin-doped nanocoral (NC650) film yielded a photocurrent density of 0.18 mA cm⁻². After Pi treatment, a 7-fold enhancement in the photocurrent density, up to 1.3 mA cm⁻² at 1.23 V_{RHE}, was achieved (Figure 2F). Like another boron-doped hematite nanowire anode (BNW650), Pi treatment created as high as 1.8 mA cm⁻² at 1.23 V_{RHE} (Figure 2G), which is among the most efficient photoanodes prepared by a hydrothermal method.¹⁰ Considering that different anodes should have different limiting factors affecting their PEC performance, the common enhancing effect of Pi treatment for all of the films suggests that this strategy is applicable to other hematite photoanodes, regardless of the structure and preparation methods used.

The effect of Pi treatment on the J – V behavior of hematite is quite different from that induced by other surface modification methods such as WOC modification (e.g., Co-Pi).^{3–5,19,29} For comparison, we also prepared a Co-Pi-modified film by the

commonly used methods.³ Consistent with earlier studies,^{3,5,19} the photoanode loaded with Co-Pi exhibited ca. 200 mV cathodic shift in the photocurrent onset potential (Figure 2A). However, the change in the onset potential was not significant for the Pi anode (Figure 2A). Loading with Co-Pi could also lower the dark current onset, as shown in Figure S8 in the SI, while all of the Pi anodes exhibited more positive dark current onset than the relative pristine anodes (Figure S8 in the SI and Figure 2C–G). Intriguingly, at higher applied potential ($>0.87 V_{\text{RHE}}$), the photocurrent density of the Pi anode became higher than that of the Co-Pi anode, and the photocurrent density at $1.23 V_{\text{RHE}}$ was nearly twice (0.30 versus 0.51 mA cm^{-2}) that of the Co-Pi anode. Because the cathodic shift in the photocurrent onset potential of the Co-Pi-modified anode is known to stem from acceleration of the interfacial hole-transfer kinetics, the different effects of Co-Pi modification and Pi treatment suggest that the interfacial hole-transfer process by Pi treatment is not sufficiently accelerated as in the case of Co-Pi modification. These observations inspired us to load the WOC Co-Pi on the surface of Pi-treated hematite films to accelerate the hole-transfer kinetics. As expected, the dual-treated photoanode exhibited a considerable decrease in the photocurrent onset relative to that of the Pi anode and a significant enhancement in the photocurrent density (Figure 2A).

The J – V scan behaviors of the Pi anodes were more similar to those of heterojunction hematite films such as $\text{MgFe}_2\text{O}_4/\text{Fe}_2\text{O}_3$, where the enhanced PEC activity is attributed to the enhanced electron–hole separation within the anodes.¹⁴ To understand the effects of Pi treatment on the electron–hole separation and hole-transfer kinetics, EIS spectra were measured under visible-light illumination. The Nyquist plots under irradiation at $1.23 V_{\text{RHE}}$ are shown in Figure 3A. It was observed that the curve of the Pi anode had a much smaller radius than that of the pristine anode, indicative of much more rapid charge-transfer kinetics in the Pi anode.³⁰ Further, we used the equivalent circuit diagram shown in Figure 3A, which has proven to be reliable in modeling the pristine and surface-modified hematite films,³¹ to fit and simulate the physical parameters associated with different processes. R_s values, which stand for all of the series resistances in the PEC cell, were not significantly altered after Pi treatment and remained nearly constant with potentials (Figure S17A in the SI), verifying the reliability of the adopted impedance-simulating circuit and fitting process. The surface hole-trapping process can be reflected by R_{trapping} and C_{trap} .³¹ Compared with those of the pristine anode, the values of R_{trapping} for the Pi anode decreased by a factor of ~ 3 – 6 (Figure 3B), indicating that the surface trapping of photogenerated holes in the Pi anode was much easier than that on the pristine films. Contrastively, it was reported that the R_{trapping} values do not vary much with the modified Co-Pi.⁵ C_{trap} also increased by a factor of ~ 3 – 5 after Pi treatment, indicative of an increased number of surface states for hole trapping in the Pi anode. For the effect of Pi treatment on the interfacial hole-transfer kinetics, we can refer to $R_{\text{ct,trap}}$. Compared with those of the pristine anode, the values of $R_{\text{ct,trap}}$ of the Pi anode decreased by a factor of 30 – 60 (Figure S17C in the SI). However, these values were much smaller than that on the Co-Pi-modified anodes (a factor of ~ 100 – 1000).⁵ These facts indicate that the oxidation of water on the surface of the Pi anode was facilitated, relative to the pristine surface, but to a lesser extent than that by Co-Pi modification, which is in well agreement with the J – V scan results in Figure 2A.

Mott–Schottky measurements were performed in the dark to determine the carrier densities of semiconductor films, as shown in Figure 3D. The carrier densities of the pristine and Pi anodes were estimated to be 1.8×10^{19} and $2.5 \times 10^{19} \text{ cm}^{-3}$, respectively. As shown, Pi treatment did not increase the carrier density of hematite films to the same extent as the normal bulk doping method (which usually increases the carrier density by a factor of 10 – 100).^{10,11} Hence, the enhancement in the PEC activity by Pi treatment cannot be mainly attributed to the increase of the electron mobility as in the normal bulk doping methods.

The increased concentration of Fe^{2+} sites and oxygen vacancies toward the surface, as shown by the GI-XANES and EXAFS results (Figures 1D and S7 in the SI), is reminiscent of the surface modification of hematite with divalent metal cations such as Mg^{2+} in which the substitution of divalent metals for Fe^{3+} would form a p-type overlayer for fabricating a p–n junction on the surface. The charge-separation efficiency can be largely improved by the generated built-in electric field crossing the junction. In our study, Fe^{2+} should play a role analogous to that of the reported Mg^{2+} ion in drawing photogenerated holes from the inner part to the surface. A unique characteristic for the gradient-structured $\text{FeO}_x(\text{PO}_4)_y$ layer on hematite highlighted in the present study is that the doping-induced built-in electric field is continuous and runs through the whole doping layer. All of the photogenerated carriers in this layer can encounter this electric field, which would force the holes to move toward the surface. Consequently, the charge diffusion length can be as long as the depth of the gradient-structured layer (about 50 nm , as shown by the XPS etching profile in Figure 1A), which is much longer than that in the pristine hematite anode (known to be 2 – 4 nm).¹ Therefore, many more holes can arrive at the photoanode surface. This argument is supported by the results of the EIS experiments, in which the decrease in fitted R_{trapping} signifies a facilitated transfer of photogenerated holes from the valence band of hematite to the surface states of the Pi anode (Figure 3B). The increase in the C_{trap} values (reflection of the amount of trapping sites on the surface states) is also consistent with an increase in the concentration of the reduced iron species and oxygen vacancies sites, which can act as trapping sites.

We also note that the presence of these trapping states is not always beneficial to the overall PEC performance. When these trapping states occur on the outermost surface where the water oxidation reaction takes place, as proposed by Sivula and co-workers,⁸ hole transfer to water can be greatly retarded. This assumption can well explain the observed initial enhancement in the photocurrent density in the steady-state PEC experiments (Figure 2B). Under the PEC conditions, the oxidative environment on the surface of the hematite film could oxidize the reduced iron species, heal much of the surface oxygen vacancies, and thereby passivate these surface recombination centers.²⁸ However, such a passivation reaction is expected to occur only on the outermost film surface (e.g., several atomic layers) because of the low temperature (room temperature), and the inner layer should remain a gradient-doped structure.

CONCLUSION

We have developed a simple, universal, and effective method for achieving high photoactivity for the PEC water oxidation of hematite photoanodes. Using phosphorous acid treatment at a low temperature, a gradient-structured $\text{FeO}_x(\text{PO}_4)_y$ layer with a

thickness of about 50 nm was in situ formed on hematite films, while the bulk hematite crystal structure remained untouched. Such a Pi-treated anode exhibited a much higher PEC efficiency for water oxidation, which was attributed to the increased hole diffusion distance in the gradient-structured overlayer due to the formation of a continuous built-in electric field.

■ ASSOCIATED CONTENT

■ Supporting Information

Plot of chopped-light experiments, Nyquist plot for EIS experiments, series resistances and capacitance derived from EIS, SEM images, XRD patterns, XPS data, and XANES and EXAFS data recorded in the fluorescence mode. This material is available free of charge via the Internet at <http://pubs.acs.org>.

■ AUTHOR INFORMATION

Corresponding Author

*E-mail: ccchen@iccas.ac.cn.

Notes

The authors declare no competing financial interest.

■ ACKNOWLEDGMENTS

Financial support from the 973 Project (Grants 2010CB933503 and 2013CB632405), the NSFC (Grants 21137004, 21273245, and 21277147) and the CAS is gratefully acknowledged. We also express many thanks to Prof. Lei Su and Dr. Ying Tong of the University of Science and Technology Beijing for their kind assistance in EIS measurement.

■ REFERENCES

- (1) Sivula, K.; Le Formal, F.; Gratzel, M. Solar Water Splitting: Progress Using Hematite ($\alpha\text{-Fe}_2\text{O}_3$) Photoelectrodes. *ChemSusChem* **2011**, *4*, 432–449.
- (2) Wang, D.; Zhang, Y.; Wang, J.; Peng, C.; Huang, Q.; Su, S.; Wang, L.; Huang, W.; Fan, C. Template-Free Synthesis of Hematite Photoanodes with Nanostructured ATO Conductive Underlayer for PEC Water Splitting. *ACS Appl. Mater. Interfaces* **2014**, *6*, 36–40.
- (3) Zhong, D. K.; Sun, J.; Inumaru, H.; Gamelin, D. R. Solar Water Oxidation by Composite Catalyst/ $\alpha\text{-Fe}_2\text{O}_3$ Photoanodes. *J. Am. Chem. Soc.* **2009**, *131*, 6086–6087.
- (4) Barroso, M.; Cowan, A. J.; Pendlebury, S. R.; Gratzel, M.; Klug, D. R.; Durrant, J. R. The Role of Cobalt Phosphate in Enhancing the Photocatalytic Activity of $\alpha\text{-Fe}_2\text{O}_3$ toward Water Oxidation. *J. Am. Chem. Soc.* **2011**, *133*, 14868–14871.
- (5) Klahr, B.; Gimenez, S.; Fabregat-Santiago, F.; Bisquert, J.; Hamann, T. W. Photoelectrochemical and Impedance Spectroscopic Investigation of Water Oxidation with “Co-Pi”-Coated Hematite Electrodes. *J. Am. Chem. Soc.* **2012**, *134*, 16693–16700.
- (6) Tilley, S. D.; Cornuz, M.; Sivula, K.; Gratzel, M. Light-Induced Water Splitting with Hematite: Improved Nanostructure and Iridium Oxide Catalysis. *Angew. Chem., Int. Ed.* **2010**, *49*, 6405–6408.
- (7) Barroso, M.; Mesa, C. A.; Pendlebury, S. R.; Cowan, A. J.; Hisatomi, T.; Sivula, K.; Gratzel, M.; Klug, D. R.; Durrant, J. R. Dynamics of Photogenerated Holes in Surface Modified $\alpha\text{-Fe}_2\text{O}_3$ Photoanodes for Solar Water Splitting. *Proc. Natl. Acad. Sci. U.S.A.* **2012**, *109*, 15640–15645.
- (8) Le Formal, F.; Tétreault, N.; Cornuz, M.; Moehl, T.; Gratzel, M.; Sivula, K. Passivating Surface States on Water Splitting Hematite Photoanodes with Alumina Overlayers. *Chem. Sci.* **2011**, *2*, 737–743.
- (9) Cesar, I.; Kay, A.; Martinez, J. A. G.; Gratzel, M. Translucent Thin Film Fe_2O_3 Photoanodes for Efficient Water Splitting by Sunlight: Nanostructure-Directing Effect of Si-Doping. *J. Am. Chem. Soc.* **2006**, *128*, 4582–4583.
- (10) Wang, G.; Ling, Y.; Wheeler, D. A.; George, K. E.; Horsley, K.; Heske, C.; Zhang, J. Z.; Li, Y. Facile Synthesis of Highly Photoactive $\alpha\text{-Fe}_2\text{O}_3$ -Based Films for Water Oxidation. *Nano Lett.* **2011**, *11*, 3503–3509.
- (11) Ling, Y.; Wang, G.; Wheeler, D. A.; Zhang, J. Z.; Li, Y. Sn-Doped Hematite Nanostructures for Photoelectrochemical Water Splitting. *Nano Lett.* **2011**, *11*, 2119–2125.
- (12) Wang, P.; Wang, D.; Lin, J.; Li, X.; Peng, C.; Gao, X.; Huang, Q.; Wang, J.; Xu, H.; Fan, C. Lattice Defect-Enhanced Hydrogen Production in Nanostructured Hematite-Based Photoelectrochemical Device. *ACS Appl. Mater. Interfaces* **2012**, *4*, 2295–2302.
- (13) Lin, Y.; Xu, Y.; Mayer, M. T.; Simpson, Z. I.; McMahon, G.; Zhou, S.; Wang, D. Growth of P-Type Hematite by Atomic Layer Deposition and Its Utilization for Improved Solar Water Splitting. *J. Am. Chem. Soc.* **2012**, *134*, 5508–5511.
- (14) Hou, Y.; Zuo, F.; Dagg, A.; Feng, P. A Three-Dimensional Branched Cobalt-Doped $\alpha\text{-Fe}_2\text{O}_3$ Nanorod/ MgFe_2O_4 Heterojunction Array as a Flexible Photoanode for Efficient Photoelectrochemical Water Oxidation. *Angew. Chem., Int. Ed.* **2013**, *52*, 1248–1252.
- (15) Jia, C. J.; Sun, L. D.; Yan, Z. G.; You, L. P.; Luo, F.; Han, X. D.; Pang, Y. C.; Zhang, Z.; Yan, C. H. Iron Oxide Nanotubes Single Crystalline Iron Oxide Nanotubes. *Angew. Chem., Int. Ed.* **2005**, *44*, 4328–4333.
- (16) Hu, X.; Yu, J. C.; Gong, J.; Li, Q.; Li, G. $\alpha\text{-Fe}_2\text{O}_3$ Nanorings Prepared by a Microwave-Assisted Hydrothermal Process and Their Sensing Properties. *Adv. Mater.* **2007**, *19*, 2324–2329.
- (17) Jia, C.-J.; Sun, L.-D.; Luo, F.; Han, X.-D.; Heyderman, L. J.; Yan, Z.-G.; Yan, C.-H.; Zheng, K.; Zhang, Z.; Takano, M.; Hayashi, N.; Eltschka, M.; Klauui, M.; Ruediger, U.; Kasama, T.; Cervera-Gontard, L.; Dunin-Borkowski, R. E.; Tzvetkov, G.; Raabe, J. Large-Scale Synthesis of Single-Crystalline Iron Oxide Magnetic Nanorings. *J. Am. Chem. Soc.* **2008**, *130*, 16968–16977.
- (18) Hu, X.; Yu, J. C. Continuous Aspect-Ratio Tuning and Fine Shape Control of Monodisperse $\alpha\text{-Fe}_2\text{O}_3$ Nanocrystals by a Programmed Microwave-Hydrothermal Method. *Adv. Funct. Mater.* **2008**, *18*, 880–887.
- (19) Zhong, D. K.; Gamelin, D. R. Photoelectrochemical Water Oxidation by Cobalt Catalyst (“Co-Pi”)/ $\alpha\text{-Fe}_2\text{O}_3$ Composite Photoanodes: Oxygen Evolution and Resolution of a Kinetic Bottleneck. *J. Am. Chem. Soc.* **2010**, *132*, 4202–4207.
- (20) Spray, R. L.; Choi, K.-S. Photoactivity of Transparent Nanocrystalline Fe_2O_3 electrodes Prepared Via Anodic Electrodeposition. *Chem. Mater.* **2009**, *21*, 3701–3709.
- (21) Briggs, D.; Seah, M. P. In *Auger and X-Ray Photoelectron Spectroscopy: Practical Surface Analysis*; Wiley: New York, 1990; Vol. 1, Appendix 1.
- (22) Wandelt, K. Photoemission Studies of Adsorbed Oxygen and Oxide Layers. *Surf. Sci. Rep.* **1982**, *2*, 1–121.
- (23) Castro, L.; Dedryvere, R.; El Khalifi, M.; Lippens, P. E.; Breger, J.; Tessier, C.; Gonbeau, D. The Spin-Polarized Electronic Structure of LiFePO_4 and FePO_4 Evidenced by in-Lab XPS. *J. Phys. Chem. C* **2010**, *114*, 17995–18000.
- (24) Fujii, T.; de Groot, F. M. F.; Sawatzky, G. A.; Voogt, F. C.; Hibma, T.; Okada, K. In Situ XPS Analysis of Various Iron Oxide Films Grown by NO_2 -Assisted Molecular-Beam Epitaxy. *Phys. Rev. B* **1999**, *59*, 3195–3202.
- (25) Mills, P.; Sullivan, J. L. A Study of the Core Level Electrons in Iron and Its Three Oxides by Means of X-Ray Photoelectron Spectroscopy. *J. Phys. D: Appl. Phys.* **1983**, *16*, 723–732.
- (26) Moulder, J. F.; Stickle, W. F.; Sobol, P. E.; Bomben, K. D. In *Handbook of X-Ray Photoelectron Spectroscopy*; Chastain, J., Ed.; Perkin-Elmer Corp.: Eden Prairie, MN, 1992; Vol. 2, pp 58–59.
- (27) Landon, J.; Demeter, E.; Inoglu, N.; Keturakis, C.; Wachs, I. E.; Vasic, R.; Frenkel, A. I.; Kitchin, J. R. Spectroscopic Characterization of Mixed Fe–Ni Oxide Electrocatalysts for the Oxygen Evolution Reaction in Alkaline Electrolytes. *ACS Catal.* **2012**, *2*, 1793–1801.
- (28) Gajda-Schranz, K.; Tymen, S.; Boudoire, F.; Toth, R.; Bora, D. K.; Calvet, W.; Gratzel, M.; Constable, E. C.; Braun, A. Formation of an Electron Hole Doped Film in the $\alpha\text{-Fe}_2\text{O}_3$ Photoanode upon

Electrochemical Oxidation. *Phys. Chem. Chem. Phys.* **2013**, *15*, 1443–1451.

(29) Zhong, D. K.; Cornuz, M.; Sivula, K.; Graetzel, M.; Gamelin, D. R. Photo-Assisted Electrodeposition of Cobalt-Phosphate (Co-Pi) Catalyst on Hematite Photoanodes for Solar Water Oxidation. *Energy Environ. Sci.* **2011**, *4*, 1759–1764.

(30) Bell, N. J.; Yun Hau, N.; Du, A.; Coster, H.; Smith, S. C.; Amal, R. Understanding the Enhancement in Photoelectrochemical Properties of Photocatalytically Prepared TiO₂-Reduced Graphene Oxide Composite. *J. Phys. Chem. C* **2011**, *115*, 6004–6009.

(31) Klahr, B.; Gimenez, S.; Fabregat-Santiago, F.; Hamann, T.; Bisquert, J. Water Oxidation at Hematite Photoelectrodes: The Role of Surface States. *J. Am. Chem. Soc.* **2012**, *134*, 4294–4302.